Journal of Materials Chemistry A

ROYAL SOCIETY OF CHEMISTRY

PAPER

View Article Online
View Journal

Check for updates

Cite this: DOI: 10.1039/d5ta07792c

Understanding the degradation process in zinc–iodine hybrid flow batteries

Přemysl Richtr, [a] David Gráf, [a] Martin Drnec,[a] Jiří Charvát,[bc] Martin Bureš,[a] Ondřej Navrátil, [a] Jaromír Pocedič,[bc] Juraj Kosek[ac] and Petr Mazúr*[ac]

Zinc–iodine hybrid flow batteries (ZIHFBs) represent promising stationary energy storage with a theoretically high volumetric capacity (>250 Ah L^{-1}). However, their broader commercialization is prevented, mainly by their short lifetime, particularly when charging to a higher areal capacity of the negative half-cell (>130 mAh cm^{-2}). In our study, we investigated the origins of the performance degradation of a lab-scale ZIHFB single-cell due to excessive charging. This is manifested by a local peak on the charging voltage profile (voltaic bulge), resulting in decreased coulombic efficiency for the subsequent battery cycling. Systematic variation of the selected experimental conditions (including charging SoC limit and electrolyte composition) and battery construction (use of non-conductive felt in individual half-cells and hydraulic shunt of electrolyte tanks), combined with *post-mortem* characterization of internal components (pressurized membrane tightness test and microtomographic evaluation of Zn distribution within the felt electrodes), revealed the origin of the performance degradation. It originates from non-homogeneous Zn deposition leading to the formation of a compact zinc layer near the electrode-membrane interface, which restricts ion supply to the rest of the 3D negative electrode. As a consequence, Zn dendrite growth towards the positive electrode is promoted, leading to membrane perforation and malfunction. With the optimized operating conditions and battery construction, we achieved stable and efficient mid-term cycling with a coulombic efficiency of ≥95% and energy efficiency of >83% at 100 mA cm^{-2}, and a low-capacity fade of 0.02% per cycle. The enhanced insight into the degradation mechanism will be further used to design effective mitigation strategies to enhance the areal capacity and durability of ZIHFBs and related zinc-based chemistry.

Received 23rd September 2025
Accepted 8th December 2025

DOI: 10.1039/d5ta07792c

rsc.li/materials-a

Open Access Article. Published on 09 December 2025. Downloaded on 23/12/2025 23:59:47.
This article is licensed under a Creative Commons Attribution 3.0 Unported Licence.

1. Introduction

Stabilization of the electricity grid is compulsory to achieve the full potential of renewable energy sources. The most widely spread types of energy storage (ES) are physical-based and electrochemical-based.[1,2] Pumped hydro energy storage (PHES), compressed air, and flywheel technologies are representatives of physical-based ES, with PHES being the most dominant among the technologies, despite low flexibility, limited availability of suitable sites, and high-investment costs. Li-ion batteries are the most dominant electrochemical ES technologies due to their high efficiency and energy density. Nonetheless, the high risk of fire and growing demand for batteries for e-mobility applications motivate the R&D of alternative systems, including redox flow batteries (RFBs). The main advantages of RFBs are safety (non-flammability due to the use of aqueous electrolytes) and flexible scalability (decoupled power and capacity).[3,4] So far, the vanadium redox flow battery (VRFB) represents the most developed system, which excels in terms of its long lifetime (up to 15 000 cycles and 20 years), easy recyclability, and residual value of electrolytes. However, high capital expenditures (CAPEX) due to the high vanadium price, and low energy density hinder its commercialization.[5–10]

As an alternative, hybrid flow batteries (HBFs) with metal deposition are being developed due to their theoretically higher energy density and abundant resources of metals such as zinc or iron. In this concept, a metal is deposited on the negative electrode during battery charging, while it is dissolved during discharging. The battery capacity is thus given by two factors: the concentration of active species dissolved in the electrolytes (volumetric capacity), and the molar amount of metal, which can be reversibly deposited within the negative half-cell (areal capacity, Q_{areal}).

Various HFB chemistries have been reported. The all-iron HFB excels in terms of its cost-effectiveness of the active materials, low environmental impact, and high safety. Conversely, a low redox potential of iron deposition promotes a parasitic hydrogen evolution reaction (HER) on the negative

[a]University of Chemistry and Technology Prague, Department of Chemical Engineering, Technicka 5, 166 28 Prague, Czech Republic. E-mail: mazurp@vscht.cz
[b]Pinflow Energy Storage, s.r.o., Křižovnická 86/6, 110 00 Prague, Czech Republic
[c]New Technologies – Research Centre, University of West Bohemia, Univerzitní 8, 306 14, Plzeň, Czech Republic

Open Access Article. Published on 09 December 2025. Downloaded on 23/12/2025 23:59:47.
This article is licensed under a Creative Commons Attribution 3.0 Unported Licence.

electrode at a relatively high rate, which is responsible for decreased coulombic efficiency and a loss of capacity as a result of a faradaic imbalance between the electrolytes. Thus, an additional recombination cell is typically needed, which increases the complexity of storage.[11]

Zinc is another popular metal often used in HFBs, with various posolyte chemistries, including the zinc–air hybrid flow battery (ZAHFB), zinc–bromine hybrid flow battery (ZBHFB), and zinc–iodine hybrid flow battery (ZIHFB). Similar to Fe-based systems, the zinc-based HFB suffers from non-homogeneous metal deposition and dendrite formation, Zn corrosion, and side reactions such as hydrogen evolution, which negatively influence the efficiency and stability of those batteries.[12] While the ZBHFB has the highest nominal OCV (1.85 V), a relatively low cost of active species, and high energy efficiency (EE), its applicability is limited due to the toxicity and high volatility of Br_2. The ZAHFB has a slightly lower nominal OCV (1.65 V), and the use of ambient air on the positive electrode makes these batteries non-toxic and cost-effective in terms of capacity. However, poor efficiency and stability of positive electrode reactions, together with the need for expensive electrocatalysis, obstruct the commercialization of these batteries. The ZIHFB has the lowest nominal OCV of 1.3 V, which is, however, compensated by a high volumetric capacity (ZnI_2 solubility goes up to 5 mol dm^{-3}) with a theoretical energy density of 167 Wh dm^{-3}. In addition, the redox kinetics of the iodine active species reaction on cheap carbon-based electrodes are faster compared to those of other halogen elements such as chlorine or bromine.[13] The electrode reactions, including their standard redox potentials, are stated below (see eqn (1)–(4)):

$$Zn^{2+} + 2e^- \rightleftharpoons Zn^0 \quad E^\circ = -0.763 \text{ vs. NHE} \tag{1}$$

$$2I^- \rightleftharpoons I_2 + 2e^- \tag{2}$$

$$I_2 + I^- \rightleftharpoons I_3^- \tag{3}$$

$$3I^- \rightleftharpoons I_3^- + 2e^- \quad E^\circ = 0.534 \text{ vs. NHE} \tag{4}$$

During the charging, zinc is deposited from solution (according to eqn (1)) and therefore the Zn^{2+} concentration decreases in the negative electrolyte, while the reaction proceeds in the opposite direction during the battery discharge. In the positive half-cell, I^- is oxidized to low-solubility I_2 during the charging (see eqn (2)), which consequently complexes with excess I^- to form highly soluble I_3^- (see eqn (3)). Thus, only two-thirds of the iodine in the electrolyte is used for the energy storage.[13] At higher states of charge (SoC), higher order polyiodides can also be formed, which makes the posolyte chemistry relatively complex. Jang *et al.*[14] reported that during charging, a compact temporary film of adsorbed I_2 can be formed on the surface of the positive electrode, which significantly increases the charge transfer resistance of the battery. This explains the observed increase in cell overpotential by more than 300 mV when charging at high current densities (>400 mA cm^{-2}). The mentioned phenomenon can significantly limit the maximal operating power densities. In addition, I_3^- has a strong oxidizing strength, which enables fast dissolution of metallic zinc (self-discharge), according to eqn (5):

$$Zn^0 + I_3^- \rightarrow 3I^- + Zn^{2+} \tag{5}$$

The negative half-cell is linked with common limitations of zinc-based HFBs, such as poor cyclability, non-homogeneous zinc deposition (including dendrite formation), zinc oxidation, and passivation by a precipitated layer of zinc oxide or parasitic HER.[15–17] These challenges can be addressed differently, *e.g.* by optimizing the hydrodynamic conditions of the flowing electrolyte,[18] application of proprietary charging protocols (*e.g.* pulse charging),[19] or applying electrolyte additives.[20,21] Q_{areal}, *i.e.* the amount of Zn that can be safely stored in a battery, is influenced (in addition to the negative half-cell geometry) by the morphology of the deposited zinc, which can occur in three different morphologies: mossy (porous), crystalline (compact), and dendritic (needle-like).[17,22] Obviously, a crystalline morphology is preferable due to its highest density and best adhesion to the electrode substrate. The nature of the morphology is known to be strongly dependent on the operating conditions (current density, electrolyte flow rate, and bulk reactant concentration), affecting the thickness of the diffusion layer close to the electrode–electrolyte interface. According to Dundálek *et al.*,[15] the morphology can be predicted by the so-called current density ratio, CDR, *i.e.* the ratio of the actual current density to the limiting one. Although low CDRs provide mossy structures, deposition close to limiting current densities promotes dendrite formation. It is worth mentioning that a limiting current strongly depends on the reactant concentration, local flow velocities, and temperature, and thus the optimal CDR can significantly vary during the cycling.

For deposition, planar substrate electrodes can be used, however, due to the limited mass transfer of the reactants (Zn^{2+}) to the electrode surface, 3D electrodes are used more often. The 3D electrode can be either metallic[23] or carbon-based,[21,24,25] the latter one being a common material in RFBs, typically in the form of a non-woven felt of graphitized polymeric fibres (graphite felt, GF). The 3D structure of GF increases the surface area available for the reaction, thus decreasing local current densities. However, with the GF electrode, it can be expected that the deposited zinc is preferentially localized closer to the membrane/separator, compared to the planar electrode, due to the higher (by one or two orders of magnitude) electronic conductivity of GF when compared to the ionic conductivity of the electrolyte.[21] Deposition of zinc closer to the membrane/separator can lead to faster penetration of zinc dendrites through the membrane, causing cell performance degradation due to the electric shortcut.

The choice of a suitable electrode separator is a very important parameter in the design of a flow battery cell/stack.[26] The separator is responsible for the mutual electronic separation of the negative and positive half-cells (preventing internal short circuit), while it enables their ionic interconnection. In most RFB systems, it also prevents mutual cross-contamination of the electrolytes. In principle, both porous separators and ion-exchange membranes (IEMs) can be used in ZIHFBs. The

 This journal is © The Royal Society of Chemistry 2025

Open Access Article. Published on 09 December 2025. Downloaded on 23/12/2025 23:59:47.
This article is licensed under a Creative Commons Attribution 3.0 Unported Licence.

porous separator, typically a thin polymeric film with small pores (units to tens of μm), significantly reduces the convective flux of the electrolytes between the individual half-cells, while enabling fast ionic transport for charge equalization during the battery operation. However, compared to IEMs, its permselectivity is much lower, which results in a lower coulombic efficiency (CE) and faster capacity fade of battery operation due to active species cross-over. The lower ion selectivity of porous separators is compensated by typically a much lower price and better mechanical and chemical stability over a long operation time. The ionic conductivity of the separator soaked in a given electrolyte is mainly given by the pore structures and thickness.[27]

IEMs are typically ion-selective polymeric separators with immobilized ionic functional groups in their structure and pore sizes in units of nm, which yield preferential transport of either anions (in the case of anion-exchange membranes (AEMs)) or cations (for cation-exchange membranes (CEMs)). Battery performance can be optimized by tuning the membrane properties such as the polarity of functional groups and their concentration (ion-exchange capacity, IEC), chemical composition of the polymer (*e.g.* length of side-chains) or thickness. Thinner membranes with high IEC are generally more suitable for efficient battery operation at high current densities, enabling fast ionic transport but lower selectivity.[13,26,28]

In ZIHFBs, the primary use of CEMs has been reported, mostly Nafion by Chemours Company, as recently reviewed by Fan, D., *et al.*[13] With CEMs, the supporting electrolyte cations, as well as the Zn^{2+} ions, can cross-over the membrane during battery operation. The concentration of Zn^{2+} ions in the negolyte decreases significantly during the battery operation due to their conversion to metallic Zn (see Fig. 2). Thus, in the case of miscible electrolytes (*i.e.* with an initial equal composition of both electrolytes), Zn^{2+} can permeate from the posolyte due to the concentration gradient. As the permselectivity of IEMs is never ideal, particularly in such highly concentrated electrolytes, minor permeation of iodide ions to the posolyte and tri-iodide ions to the negolyte can also take place, resulting in reduced CE due to Zn oxidation (self-discharging by tri-iodides, according to eqn (5)).

The properties of the separator used can significantly affect the battery performance and lifetime, particularly the issues related to the internal short circuit caused by the growth of the zinc dendrites during battery charging, which is a common problem for zinc-based batteries. In general, larger pores of porous separators, when compared to IEMs, should simplify these degradation phenomena. Interestingly, Xie *et al.*[29] reported the use of a polyolefin-based separator with high ion conductivity, showing stable ZIHFB operation due to the so-called self-healing effect. This effect can be described as a self-discharge reaction of I_3^- with zinc dendrites that have grown into the pores of the separator, which results in continuous dendrite dissolution (according to eqn (5)) without deterioration of the battery performance, just for the price of lower CE. To further improve the ZIHFB, Xie *et al.*[30] manufactured a composite membrane by applying a thin layer of Nafion polymer on the previously used polyolefin porous separator to enhance the permselectivity of the separator. Due to the application of a thin Nafion layer, the CE was increased by 11% when compared to the cell with a pristine separator, due to reduced I_3^- cross-over from the posolyte. The single cell with the composite membrane showed stable performance at 80 mA cm^{-2} for 500 cycles without any efficiency or capacity decay.

Kellamis *et al.*[21] demonstrated enhanced battery performance thanks to the use of a gluconate electrolyte additive together with the use of a non-conductive polymeric felt (NCF) on each side of the battery cell. The use of NCF in the negative half-cell and the addition of NCF to the positive one (combination of conductive GF and NCF on the positive side) together with the implementation of the electrolyte additive led to the increased Q_{areal} from 60 mAh cm^{-2} (obtained with a standard flow battery construction) to 350 mAh cm^{-2} (at the beginning of the experiment; after 4 cycles the capacity was 280 mAh cm^{-2}) at a current density of 100 mA cm^{-2}, with 53% voltaic efficiency (VE). The addition of potassium gluconate prevented dendrite formation but also decreased the ionic conductivity of the electrolyte, which resulted in decreased VE. More importantly, the presence of NCF in the positive half-cell prevented the formation of electric shorts caused by Zn dendrites. A battery of the same construction, but without the additive, achieved an initial Q_{areal} of 480 mAh cm^{-2}; however, after 8 cycles it dropped to 370 mAh cm^{-2}. Omission of the additive resulted in an increase of VE by approximately 8% under the given conditions. The authors demonstrated a significant increase in available Q_{areal} for the ZIHFB at a reasonable current density of 100 mA cm^{-2}, which allows a significant decrease in battery stack price.

The ZIHFB shows great potential for highly effective and energetically dense stationary storage, and several recent publications have shown a potential for successful scale-up. However, commercialization of current ZIHFBs is still limited by low Q_{areal} of the negative battery half-cell.[21] When the critical amount of Zn is deposited, battery charging overvoltage gradually increases, which is eventually followed by its sudden drop upon further charging. This behaviour, manifested by a "voltaic bulge" on the charging voltage profile, leads to irreversible battery performance degradation, and this has been, to some extent, already reported in the literature,[21,31] however, without adequate effort for a deeper understanding of the phenomena's origins and mechanisms. In most cases, its presence is simply avoided thanks to sufficiently low charging voltage or capacity limit. The problem has been briefly reported by Kellamis *et al.*,[21] stating that the increased charging overvoltage is mostly related to increased mass transfer polarization, while the subsequent overvoltage drop is directly linked to the internal short circuit of the battery by the deposited Zn. However, to the best of our knowledge, a sufficiently detailed description of the voltaic bulge phenomenon, its origins, and exact degradation mechanism is still missing, thereby limiting the ability to improve battery performance at increased Q_{areal}.

In our study, we provide deeper insight into the voltaic bulge phenomena through a complex and systematic investigation combining lab-scale single-cell experiments and *post-mortem* analysis of the battery components, enabling the identification of the origins of the observed performance deterioration at

Open Access Article. Published on 09 December 2025. Downloaded on 23/12/2025 23:59:47.
This article is licensed under a Creative Commons Attribution 3.0 Unported Licence.

increased Q_{areal} and the proposal of a realistic degradation mechanism and rational mitigation strategies for performance and stability enhancement. Our study is divided into three parts describing: (i) the identification of individual degradation phenomena, (ii) evaluation methods for the recovery of the battery performance and mitigation of the degradation process, and (iii) optimization of battery construction and operation to achieve stable and efficient mid-term battery performance, achieving CE > 96% and VE > 87%, at 100 mA cm^{-2} for 70 cycles with negligible capacity decay (0.02% per cycle).

2. Experimental

2.1 Construction of the flow cell and general conditions

ZIHFB characterization was conducted using a single cell (construction derived from a standard lab-cell by Pinflow energy storage, s.r.o.). The single-cell design (see Fig. S1a) was adjusted for the needs of the ZIHFB (*i.e.* modification of the flow field design) in cooperation with Pinflow. It consists of aluminium end plates, copper current collectors, composite carbon-polymer plates, graphite felts (GFs, rayon-based), elastomeric polyolefin-based flat gaskets, electrolyte distribution frames made of PVC, and activated CEM. GF was activated according to Mazúr *et al.*[32] and the compression ratio (CR) was set to 25%. The geometric area of the electrodes was 20 cm^2 (4 × 5 cm^2). Flow-through distribution of electrolyte was used for both half-cell compartments.

The standard apparatus (see Fig. S1b) for characterization with a ZIHFB consists of a peristaltic pump (Watson-Marlow 323), two separate electrolyte tanks, and PTFE tubing that connects the tanks to the cell. The standard characterization negolyte tank contained 0.07 dm^3 and the posolyte 0.08 dm^3 of an electrolyte solution composed of 1 mol dm^{-3} of ZnI_2, 4 mol dm^{-3} of KI and 1.5 mol dm^{-3} of KCl. In some experiments, different volumes of electrolytes with the same composition were used, and this is clearly marked in a corresponding experiment. In others, the posolyte was used without Zn^{2+} ions, so the composition was as follows: 4 mol dm^{-3} of KI and 1.5 mol dm^{-3} of KCl. The flow rate of both electrolytes was set at 0.08 dm^3 min^{-1}. The entire testing apparatus was placed in a temperature-insulated box maintained at a temperature of 40 °C.

2.1.1 Construction modifications of the ZIHFB. To investigate the mechanism of irreversible battery performance deterioration, two different strategies were tested: (i) a hydraulic connection between the electrolyte tanks (short hydraulic shunt, HS, by a thin capillary positioned on the bottom of both tanks), to maintain the same levels of both electrolytes during the experiment; and (ii) a combination of electronically conductive GF and NCF (polymeric non-conductive felt, FINET PES 1 mm, MITOP) in each half-cell (see Fig. S2).

2.2 Electrochemical characterization of the ZIHFB

For the characterization of the ZIHFB single-cell, we used a complex procedure consisting of electrochemical impedance spectroscopy (EIS) and galvanostatic charge–discharge cycling, combined with constant voltage discharge, using the battery cycler BSC-815 (Biologic). In the monitoring apparatus Tevomet TV16 multichannel voltage monitor was added (Kolibrik.net (https://www.kolibrik.net/en)), which enabled online monitoring of potentials and pressure drop measurements. Each characterization procedure was slightly different; thus, we will divide this chapter into more sub-chapters.

2.2.1 Standard ZIHFB characterization. First, the ZIHFB was cycled in the SoC range of 0–20% (SoC of the negolyte), and several cycles were performed. The SoC range was then increased by 20% increments (*i.e.* a 0–40% SoC range), with cycling repeated at each step, until the battery was cycled up to 80% of the theoretical capacity of the 0.07 dm^3 negolyte. In this article, we will refer to the SoC as the ratio of the current charged capacity to the theoretical capacity of the negolyte, which corresponds to the total amount of Zn^{2+} ions. The battery was always charged galvanostatically (CC) at a current density of 100 mA cm^{-2} to a chosen SoC limit and back-discharged in a combined galvanostatic–potentiostatic (CC–CV) mode with a discharge voltage limit of 0.1 V, until the discharged current decreased below 10% of the charging current. Subsequently, several dozen cycles were performed with the charging SoC limit of 80%. From the charge–discharge cycling, the efficiencies (CE, VE, and EE) and capacity utilization (CU) were evaluated according to standard relationships[32] together with their mean values from each SoC range. CU was calculated with respect to the theoretical capacity of the negolyte according to Faraday's law.

2.2.2 Detailed ZIHFB characterization. Detailed battery characterization was performed using two different modes of EIS measurement. In the first case, the battery was gradually charged in steps with varying capacities (around the area of interest, the capacity of the step was 1.5 mAh cm^{-2}) and between each step, the EIS at OCV (further referred to as $PEIS_{OCV}$) was measured in a potentio mode, with a frequency ranging from 10 kHz to 25 mHz with a sinus amplitude of the perturbing signal of 20 mV. This was done using the BSC-815 battery cycler (Biologic). In the second case, the EIS was measured under a constant current density load (100 mA cm^{-2}) in a galvano mode (marked $GEIS_{LOAD}$) in the frequency range from 100 kHz to 50 mHz with a multi-sine regime, and the amplitude of the perturbing signal was 12.5 mA cm^{-2}. This was done with a potentiostat VSP-3e (Biologic), enabling measurements in a broader frequency range. As the EIS was measured under current load, the battery was continuously charged (or discharged) during the impedance measurement.

From the EIS experiments, the values of area specific resistances (ASRs) were evaluated; the ohmic ASR (ASR_Ω) and charge transfer ASR (ASR_{CT}) by fitting the EIS spectra to a suitable equivalent circuit model (for equivalent circuit, see Fig. S3a). All EIS spectra are presented as Nyquist plots, with the direction of the frequency indicated from a high frequency closer to the *y*-axis to a low frequency towards the right (see Fig. S3b).

2.2.3 Strategies for capacity regeneration and stable operation of the ZIHFB. The rest of the experiments consisted of the electrochemical characterization techniques mentioned above. Volumes of the electrolytes can differ, and some construction

 This journal is © The Royal Society of Chemistry 2025

Open Access Article. Published on 09 December 2025. Downloaded on 23/12/2025 23:59:47.
This article is licensed under a Creative Commons Attribution 3.0 Unported Licence.

modifications were realized (*i.e.* HS of electrolyte tanks or implementation of NCF into the cell), which have been described in Section 2.1.1.

2.2.3.1 Electrolyte remix. Capacity regeneration in RFBs can be carried out by the electrolyte mixing procedure (so-called electrolyte remix) to restore the initial electrolyte composition. Electrolyte remix was performed after the ZIHFB was fully discharged (*i.e.* after combined CC–CV discharge with potentiostatic retention at 0.1 V). Subsequently, the outlet tubes connecting the individual half-cells to the respective electrolyte reservoirs were interchanged, and in this arrangement, the electrolytes were intensively mixed (30 min) in order to achieve full equalization of their composition and possible additional complete dissolution of zinc residues in the negative half-cell by their reaction with tri-iodide ion residues contained in the posolyte. Subsequently, the outlet tubes were reconnected to the respective reservoirs, and the electrolytes were distributed in an equal volume ratio to the respective reservoirs.

2.2.3.2 Stable electrochemical operation conditions. A cycling protocol with 10 CC cycles followed by two CC (charging) and combined CC–CV (discharging) formatting cycles (CV cut-off voltage of 0.1 V until the discharge current was <10% of the charge current) was deployed, ensuring full discharge of the negative half-cell and complete zinc dissolution. To secure safe operating conditions during the mid-term cycling stability, the charging limit was limited to 50% (negolyte volume of 0.06 dm^3, Q_{areal} of 80 mAh cm^{-2}), *i.e.*, safely below the critical capacity. Charging was terminated either upon reaching this capacity or a cell voltage of 1.55 V.

2.3 Microstructure analysis of negative electrodes

Confocal optical observations were performed using a laser scanning confocal microscope (LSCM, Keyence VK-X3000). Although the instrument is equipped with a 404 nm semiconductor laser, all images in this study were acquired using the integrated white-light LED illumination source. Depending on the region of interest, the imaging parameters were adjusted as follows: a 2.5× objective lens (NA = 0.075) with an optical zoom of 0.7 and a pitch of 40.00 μm, or a 20× objective lens (NA = 0.46) with an optical zoom of 1.0 and a pitch of 0.84 μm. All measurements were performed at a brightness setting of 82.

The microstructure of the selected GF with deposited zinc was studied by micro-computed tomography (μCT, sample size 50 × 40 × 5.5 mm). The samples were scanned using an X-ray microtomograph, CT portable 160.90 (Fraunhofer). An accelerating voltage of 90 kV was used for the scanning, and 3500 images were taken for each scan with a resolution of 22.19 microns per pixel and an exposure time of 450 ms per image. The total scanning time was five hours per sample. The resulting structure was obtained from the captured images by mathematical reconstruction in the native microtomograph software.

To evaluate porosity changes in the negative electrode using μCT data, the original TIFF scans were first processed by rescaling the intensity values in the range of 0 to 1. These values were then normalized using a power-law transformation, specifically by taking the fourth root of the intensity, which helped to enhance the contrast and reduce the influence of extreme values. The resulting intensity values were further normalized so that their sum equalled one, ensuring proportional distribution across the volume.

To estimate the amount of zinc deposited in the electrode, the experimental capacity was converted to mass using Faraday's law (assuming 100% current yield) and then to the molar mass of zinc. The volume of deposited zinc was calculated by dividing this theoretical Zn mass by the density of metallic zinc and correcting it for effective zinc density, assumed to be 0.7 (of metallic zinc) based on the literature.[33] This total zinc volume was then distributed throughout the 3D μCT volume proportionally to the normalized intensity, resulting in a spatial zinc volume map. The porosity was calculated voxel-wise according to the equation below:

$$\theta = 1 - \frac{(1 - \theta_{GF})\mathrm{d}V + V_{3D\_zinc}}{\mathrm{d}V} \quad (6)$$

where θ_{GF} is the initial porosity of the felt, V_{3D_zinc} is the zinc volume in the voxel, and $\mathrm{d}V$ is the voxel volume. Although the original voxel resolution was 22.19 micrometers, for statistical evaluation, the data were aggregated into blocks of 100 × 100 × 4 voxels, resulting in an effective voxel size of approximately 2.2 mm × 2.2 mm × 0.1 mm.

Finally, porosity values were averaged across *XY* slices spanning the electrode thickness, from the membrane to the current collector, to observe spatial trends and correlate them with the state of charge and structural changes in the electrode.

2.4 Half-cell tightness pressure test

To assess the tightness of the battery half-cell, a pressure decay test was carried out in a specialized set-up (see Fig. S4). One of the half-cells was pressurized by nitrogen applying a selected overpressure (in the range of 100–600 mbar), then the hydraulic circuit was closed, and a decay of the internal pressure was monitored by the pressure sensor. The internal tightness of the battery was assessed from the slope of pressure decrease with time, evaluated from 5-minute interval measurements.

3. Results

The primary aim of this study was to obtain a better understanding of the phenomena taking place during the operation of a ZIHFB, particularly during its charging at increased Q_{areal}, leading to irreversible degradation of the battery performance. The results section is divided into three parts: (i) identification of the individual degradation phenomena, (ii) testing methods for battery performance recovery and the mitigation of the degradation process, and (iii) identification of safe operating conditions providing stable and efficient battery performance at the mid-term time scale.

3.1 Voltaic bulge

3.1.1 Existence of a voltaic bulge in the ZIHFB. In this section, we present the experiments in which the ZIHFB single-

Open Access Article. Published on 09 December 2025. Downloaded on 23/12/2025 23:59:47.
This article is licensed under a Creative Commons Attribution 3.0 Unported Licence.

cell was cycled with a stepwise increasing SoC charging limit (to 20, 40, 60, and 80% of the theoretical capacity of the negolyte, with a volume of 0.07 mol dm^{-3}) in order to assess the maximum Q_{areal} still providing efficient and stable operation. Subsequently, several dozen charge–discharge cycles were performed with an 80% SoC charging limit.

First, at low SoC charging limits (20 and 40% SoC), the battery achieved high efficiencies (see Table 1), with CE above 98% and EE above 85%. EE started to decrease during cycling with a 60% SoC charging limit, but the CE remained above 98%. The decrease of the EE was primarily caused by increasing charging voltage around 100 mAh cm^{-2} (corresponding to approx. 50% SoC of the negolyte). When increasing the charging limit to 80% SoC (~150 mAh cm^{-2}), a sharp increase of the cell voltage appeared, followed by its sudden drop, demonstrating a voltaic bulge around 125 mAh cm^{-2} (see Fig. 1a). After the bulge, the charging voltage remained relatively high, around 1.5 V, until the end of the charging half-cycle. Interestingly, the initial discharge voltage was about 100 mV lower than for a 60% SoC charging limit, suggesting increased internal resistance of the discharging cell. The resulting CE of the cycle was significantly lower (by 9%) when compared to lower charging SoC limits. As visible from Fig. 1a, the available discharge capacity was only slightly higher than the value corresponding to the position at the end of the bulge on the *x*-axis, despite the fact that the cell discharging included a potentiostatic step at a low cell voltage of 0.1 V. This indicates the occurrence of some irreversible processes during the previous charging. During the subsequent battery cycling within the same SoC range, the voltaic bulge on the charging voltage profile gradually disappeared (see Fig. 1b and c). Nonetheless, CE continuously decreased from 85% to 70% (see Fig. 1d). Additionally, we observed a distorted charging voltage profile at the bulge position, indicating an internal short circuit of the battery (see the green curve in Fig. 1c). The observed CE decay can be, to some extent, caused by a change of electrolyte composition and volume due to the observed net-flow through the CEM by osmosis and electro-osmosis (a detailed description of expected ion fluxes in our system is further discussed in this chapter). However, the main cause of performance deterioration seems to be most likely linked to the failure of inner cell components.

3.1.2 Expected ion fluxes in our ZIHFB. For the sake of a better understanding of the voltaic bulge in the battery, we provide a detailed discussion of the expected fluxes of the individual electrolyte constituents (ions and water), which play a significant role in the observed degradation mechanism, and, thus, it is important to describe them specifically for our electrolyte composition (*i.e.* beyond the discussion in the Introduction).

In a ZIHFB cell employing a CEM, potassium ions serve as the primary charge carriers. During battery charging, they migrate, accompanied by water molecules in their hydration shells, from the posolyte to the negolyte under the influence of the electric field[34] to maintain electroneutrality in the electrolytes. A minor flux of Zn^{2+} ions to the negolyte may also occur; however, this contribution is significantly smaller due to their larger size.[34] In the positive half-cell, iodides are oxidized to tri-iodides. The reduced concentration of iodides in the posolyte promotes their diffusion from the negolyte, whereas tri-iodide ions can diffuse in the opposite direction. Nevertheless, the transport of both anions is strongly suppressed by the CEM due to its high selectivity and Donnan exclusion. During charging, water is transported predominantly to the negolyte, driven by both electro-osmotic drag associated with K^+ migration and by osmotic pressure differences arising from compositional changes during charging (schematics of all fluxes are shown in Fig. 2). Although all fluxes theoretically reverse during discharge, complete compensation of species transport is rarely achieved in practice, and the extent of reversal strongly depends on operating conditions, including the ratio of charging to discharging current densities (which governs migration), the duration of idle periods, and the SoC range used for the battery cycling. Consequently, the volumes of the negolyte and posolyte change dynamically during battery operation. Importantly, because the charging processes are not fully efficient (due to self-discharge, parasitic hydrogen evolution reaction, passivation *etc.*), the net ionic and water flux through the CEM is biased towards the charging direction. Thus, over-extended cycling, this imbalance leads to progressive electrolyte overflow towards the negolyte.

3.1.3 Structural analysis of the negative 3D electrode. When analysing the negative felt electrode after the standard deposition to 80% SoC (negolyte volume of 0.06 dm^3, Q_{areal} of 129 mAh cm^{-2}), the zinc was visibly deposited on both sides of the GF, *i.e.* on the side facing the current collector (see Fig. S5b) as well as on the side facing the membrane (see Fig. 3a). The zinc distribution within the GF obtained *via* detailed μCT characterization (see Fig. 3b and c) confirmed its dominant deposition within a relatively thin region neighbouring the membrane. The compactness of the layer on the current collector side is clearly visible from confocal laser optical microscopy images (Fig. 3d). Some holes are also present within the layer, showing that the fibres of the GF are compactly covered by the Zn layer.

The preferential distribution of Zn close to the membrane is because the electronic path within the GF is by an order of magnitude more conductive (1100 mS cm^{-1},[35] depending on the relative compression) when compared to the ionic conductivity of the electrolyte (300 mS cm^{-1}). Thus, the electric charge is preferentially transported in the form of electrons to the

Table 1 Mean efficiencies and capacity utilization values. Experimental conditions: standard electrolyte composition; electrolyte volume: 0.07 dm^3 negolyte, 0.08 dm^3 posolyte; current density of 100 mA cm^{-2}. Operating temperature: 40 °C; electrolyte flow rate: 0.08 dm^3 min^{-1}

SoC charging limit	Number of cycles	CE %	VE %	EE %	CU %
20% SoC	5	99.1	84.5	83.7	20
40% SoC	5	98.8	85.4	84.4	40
60% SoC	5	98.7	78.4	77.4	59
80% SoC	5	89.4	76.4	68.2	72
80% SoC	49	77.0	78.0	60.0	67

This journal is © The Royal Society of Chemistry 2025

Open Access Article. Published on 09 December 2025. Downloaded on 23/12/2025 23:59:47.
This article is licensed under a Creative Commons Attribution 3.0 Unported Licence.

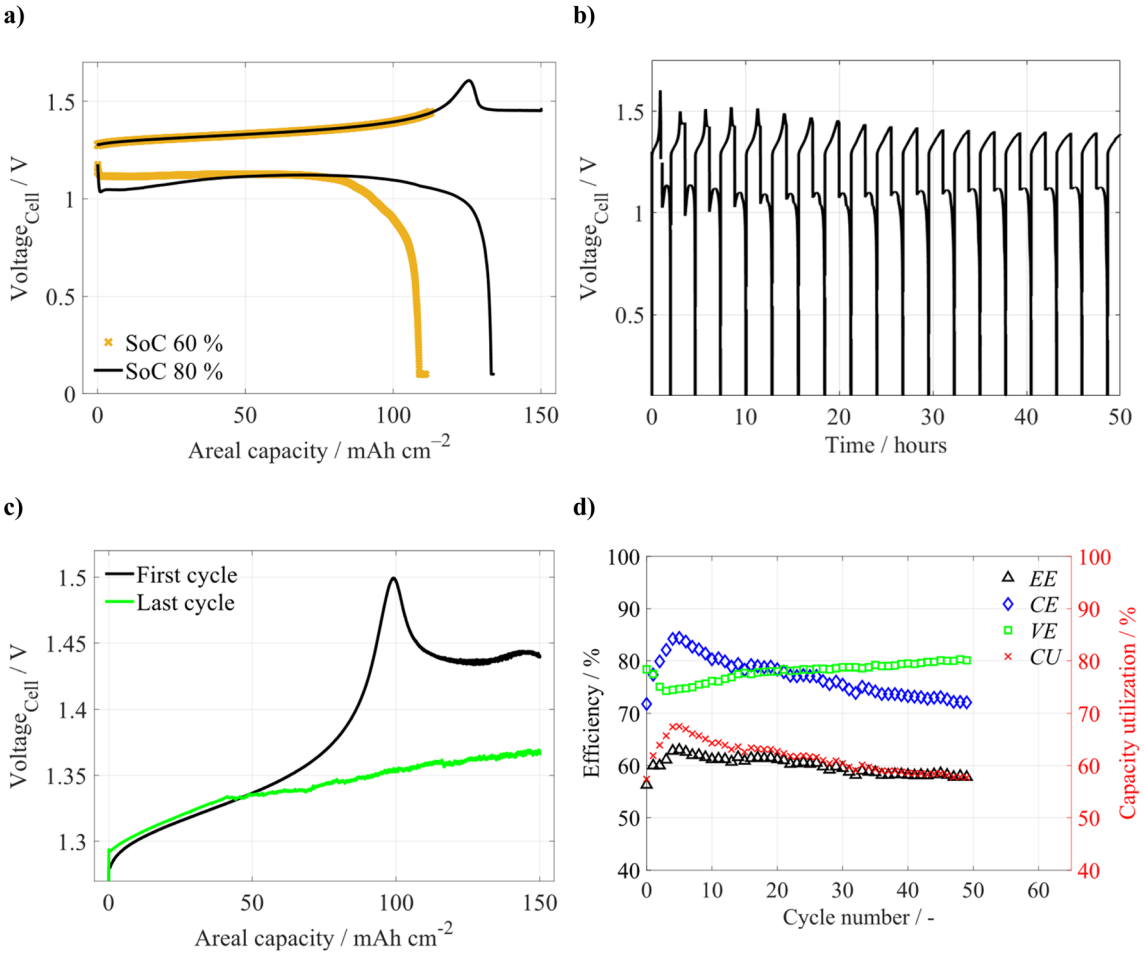

Fig. 1 (a) U-Q_{areal} dependence for 60% and 80% SoC charging limit. Subsequent battery cycling (49 cycles) with 80% SoC charging limit: (b) cell voltage development during the initial 20 cycles; (c) U-Q_{areal} dependence comparing charging for the 1st and last cycle. (d) Evolution of efficiencies and CU. Experimental conditions: standard electrolyte composition; electrolyte volume: 0.07 dm^3 of negolyte, 0.08 dm^3 of posolyte; current density: 100 mA cm^{-2}. Operating temperature: 40 °C; electrolyte flow rate: 0.08 dm^3 min^{-1}.

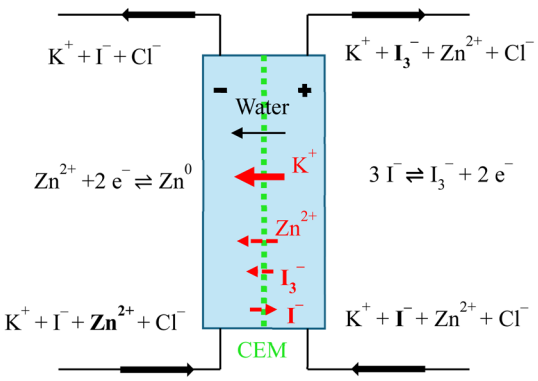

Fig. 2 Expected cross-flow of ions during ZIHFB charging for the initial equal electrolyte composition.

proximity of the membrane, where it is transferred from carbon fibres to an electrolyte *via* electrochemical reaction of Zn deposition. As expected, more zinc is deposited at the inlet of the GF due to the higher local concentration of Zn^{2+} reactants in the inlet region, which are gradually consumed by the charging reaction. More importantly, excess Zn deposition close to the membrane gradually decreases the effective area available for ionic transport through the membrane required for maintaining the electrolyte electroneutrality, as discussed in the previous chapter. μCT analysis revealed that the negative electrode porosity in the region near the membrane (0–0.09 mm) decreased from 0.935 (initial porosity of the GF according to ref. 36) to ~0.30 (under the conditions without an observable voltaic bulge) and further to 0.15 under bulge conditions. This is consistent with the observed increase in ASR_{CT} due to reduced ionic transport through this progressively thicker and more compact layer adjacent to the membrane. A more detailed discussion is presented in Section S1 (and Fig. S6) in the SI.

At a certain Q_{areal} the transport of the ions becomes limited by the created compact zinc layer on the GF-membrane interface, and thus the overpotential of the cell steeply increases. Once the peak overvoltage is achieved, it starts to decline, most probably due to gradual piercing of the CEM by Zn dendrites, which are growing from the compact Zn layer towards the

Open Access Article. Published on 09 December 2025. Downloaded on 23/12/2025 23:59:47.
This article is licensed under a Creative Commons Attribution 3.0 Unported Licence.

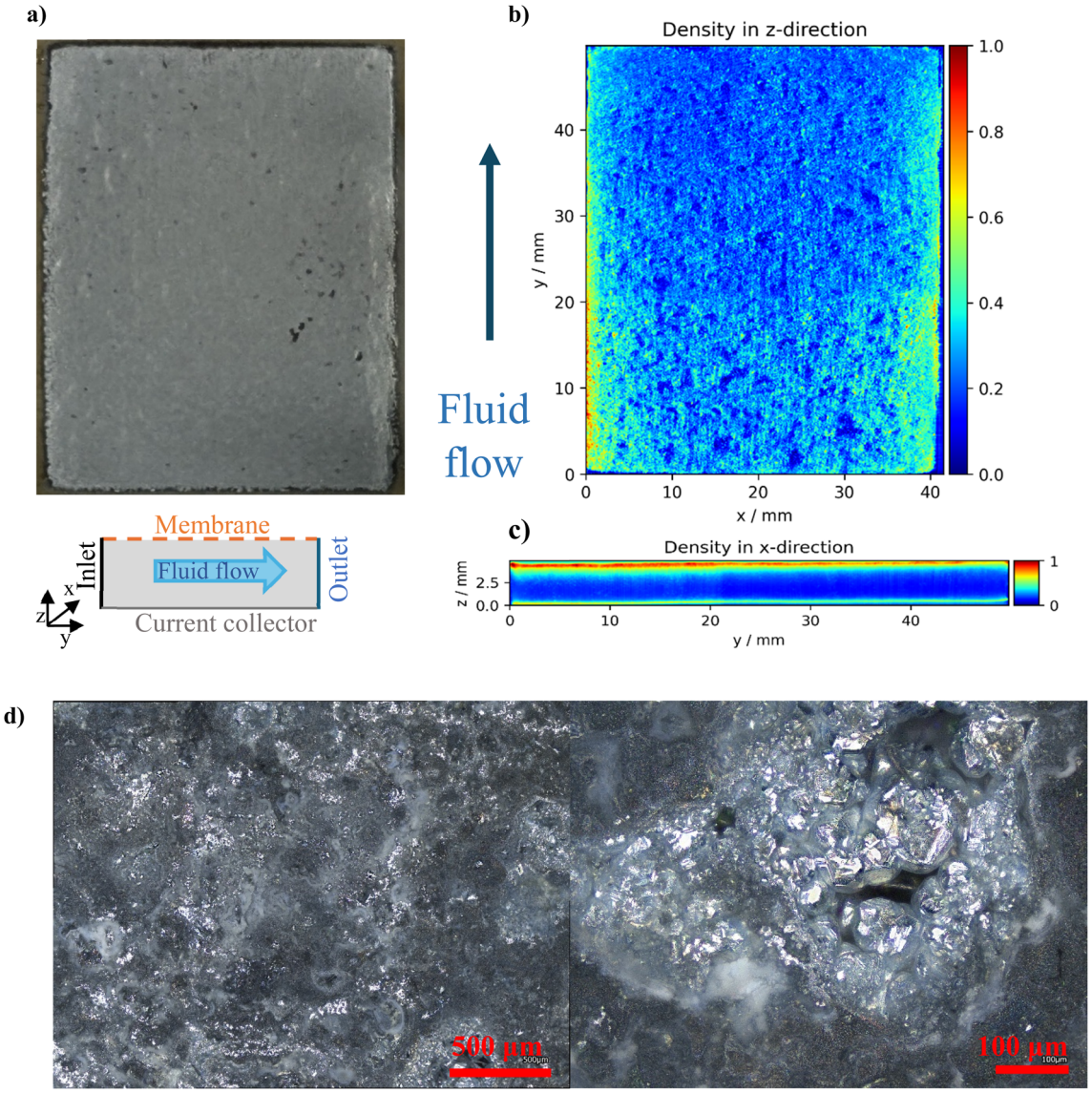

Fig. 3 (a) Photograph of GF covered with zinc on the membrane side; µCT reconstruction in the (b) *z*- and (c) *x*-direction showing the Zn distribution within the GF electrode. (d) Detail of a confocal laser microscopy image showing the compact zinc layer deposited at the electrode-membrane interface.

positive electrode. Interestingly, the cell voltage does not drop to zero (nor close to this value), which would be expected for a short-circuited cell, but it only decreases to a value slightly below 1.5 V. This can be explained by the immediate exposure of zinc dendrites to tri-iodide ions contained in the charged posolyte, which effectively dissolves these temporary shorts. This so-called self-healing effect in the ZIHFB has been described by Xie *et al.*[29] for the cell configuration using a porous separator, where it effectively prevented a short circuit of the cell. In contrast, for a cell using homogeneous CEM, the growing Zn dendrites can pierce the membrane (which is much thinner and more compact compared to the separator), resulting in membrane perforation and battery performance deterioration. The presence of tri-iodides in the posolyte thus no longer has a self-healing effect as reported for cells using a porous separator.

Overall, the gradual accumulation of Zn within the thin compact layer near the membrane, associated with a decrease in the negative electrode porosity, and resulting ionic transport limitation leads to a sharp increase in ASR_{CT}, membrane perforation by growing dendrites, and eventual irreversible performance deterioration.

3.2 Detailed study of the voltaic bulge

To further investigate the origins of the voltaic bulge, the reference electrodes were positioned on the outlet of both half-cells, allowing online monitoring of both electrodes' potentials during the battery testing. The potentials were recalibrated to the normal hydrogen electrode (NHE). In Fig. S7, we can see that

 This journal is © The Royal Society of Chemistry 2025

Open Access Article. Published on 09 December 2025. Downloaded on 23/12/2025 23:59:47.
This article is licensed under a Creative Commons Attribution 3.0 Unported Licence.

during the battery charging within the voltaic bulge capacity region, the electrode potentials showed only a minor change in their trends, not proportional to the increase in the observed cell voltage. This can be illustrated by a difference between the measured cell voltage (yellow curve) and the calculated difference between both electrodes' potentials (purple curve). This suggests that the increased cell overvoltage is associated with processes related to the CEM rather than the electrodes.

First, we wanted to confirm that the presence of a voltaic bulge is not a function of electrolyte SoC (*i.e.* composition). Thus, we performed a single charge–discharge experiment with two different volumes of negolyte: (i) a standard negolyte volume of 0.07 dm^3 (Q_{areal} of 150 mAh cm^{-2}), and (ii) a decreased volume of 0.05 dm^3 (Q_{areal} of 107 mAh cm^{-2}). As expected with the decreased negolyte volume, we did not observe signs of the voltaic bulge (see Fig. 4a) when charging to the same SoC limit (80% of the negolyte's theoretical capacity). We compared ASR_{Ω} and ASR_{CT} evaluated from EIS measurements performed at various SoCs within these experiments. We can see that at the beginning of the charging, ASR_{Ω} slightly decreases for both negolyte volumes, but a significant increase in ASR_{CT} occurs only for the standard (higher) negolyte volume (see Fig. 4b). In contrast, with the lower negolyte volume, there is only a minor ASR_{CT} increase at the very end of the charging. For a lower negolyte volume, both ASRs remain almost constant during the whole discharge period, and they increase only at the end of discharging (see Fig. 4c). Based on these observations, we can clearly state that the voltaic bulge is not a function of electrolyte composition but is directly related to the amount of deposited Zn. For the standard negolyte volume, the development of ASRs is significantly different and will be further discussed within this chapter. Note: as described in previous paragraphs, the increased cell polarization is only partially related to electrode processes (shown in Fig. S7). Thus, other observed changes related to the ASR_{CT}, *i.e.* impedance in the medium frequency range, most likely originate from a complex interplay of several processes, as will be further discussed. Despite this, for the sake of simplicity, we will refer to them as ASR_{CT}.

Detailed characterization of the voltaic bulge for the standard negolyte volume was carried out by stepwise charging, where between each charging step (approx. 1.5 mAh cm^{-2} within the region of the voltaic bulge) the $PEIS_{OCV}$ was measured. In Fig. 5a, we can see that the charging voltage in the region of the bulge is significantly higher when compared to the standard charging (*i.e.* CC charging without frequent EIS

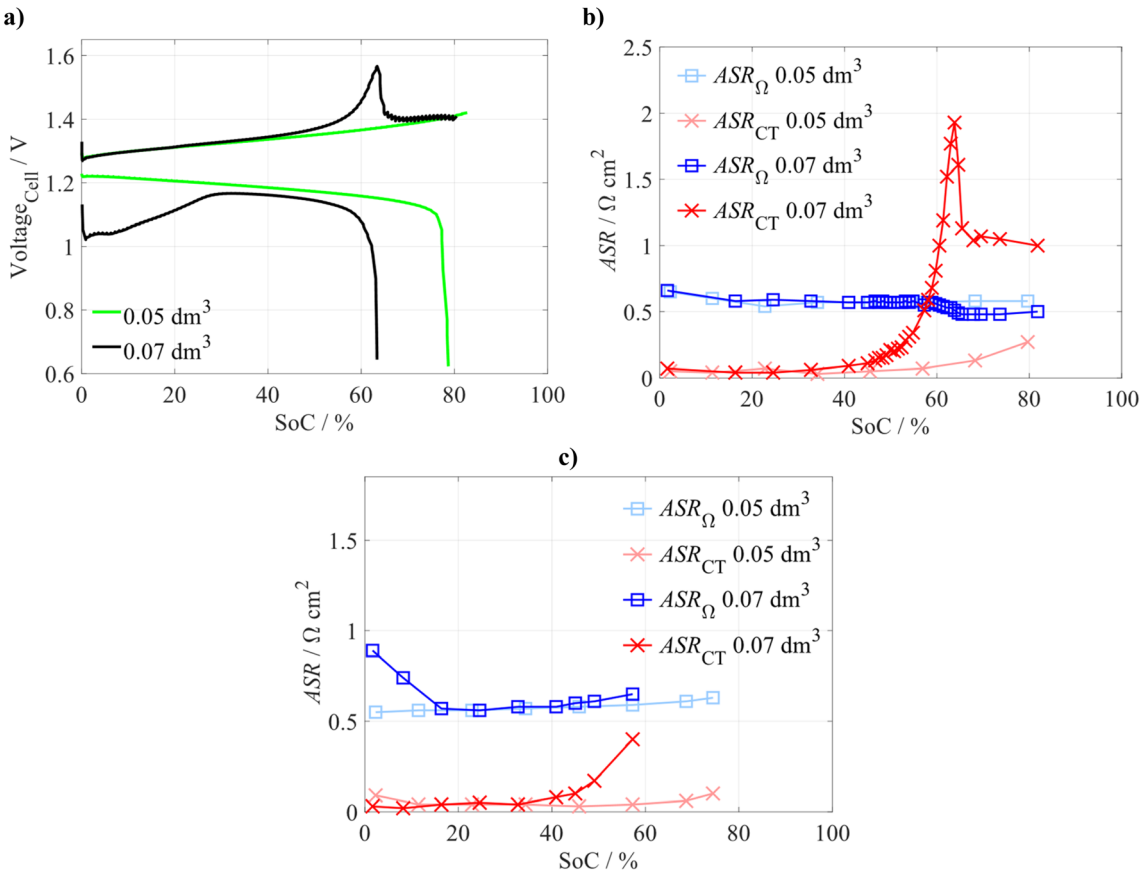

Fig. 4 (a) U-Q_{areal} dependence of a charge–discharge cycle for two different negolyte volumes with the same 80% SoC charging limit; ASR_{CT} and ASR_{Ω} evaluated from $GEIS_{LOAD}$ measured for the battery for the (b) charging and (c) discharging phase of the initial cycle. Experimental conditions: standard electrolyte composition, current density: 100 mA cm^{-2}; operating temperature: 40 °C; electrolyte flow rate: 0.08 dm^3 min^{-1}.

Open Access Article. Published on 09 December 2025. Downloaded on 23/12/2025 23:59:47.
This article is licensed under a Creative Commons Attribution 3.0 Unported Licence.

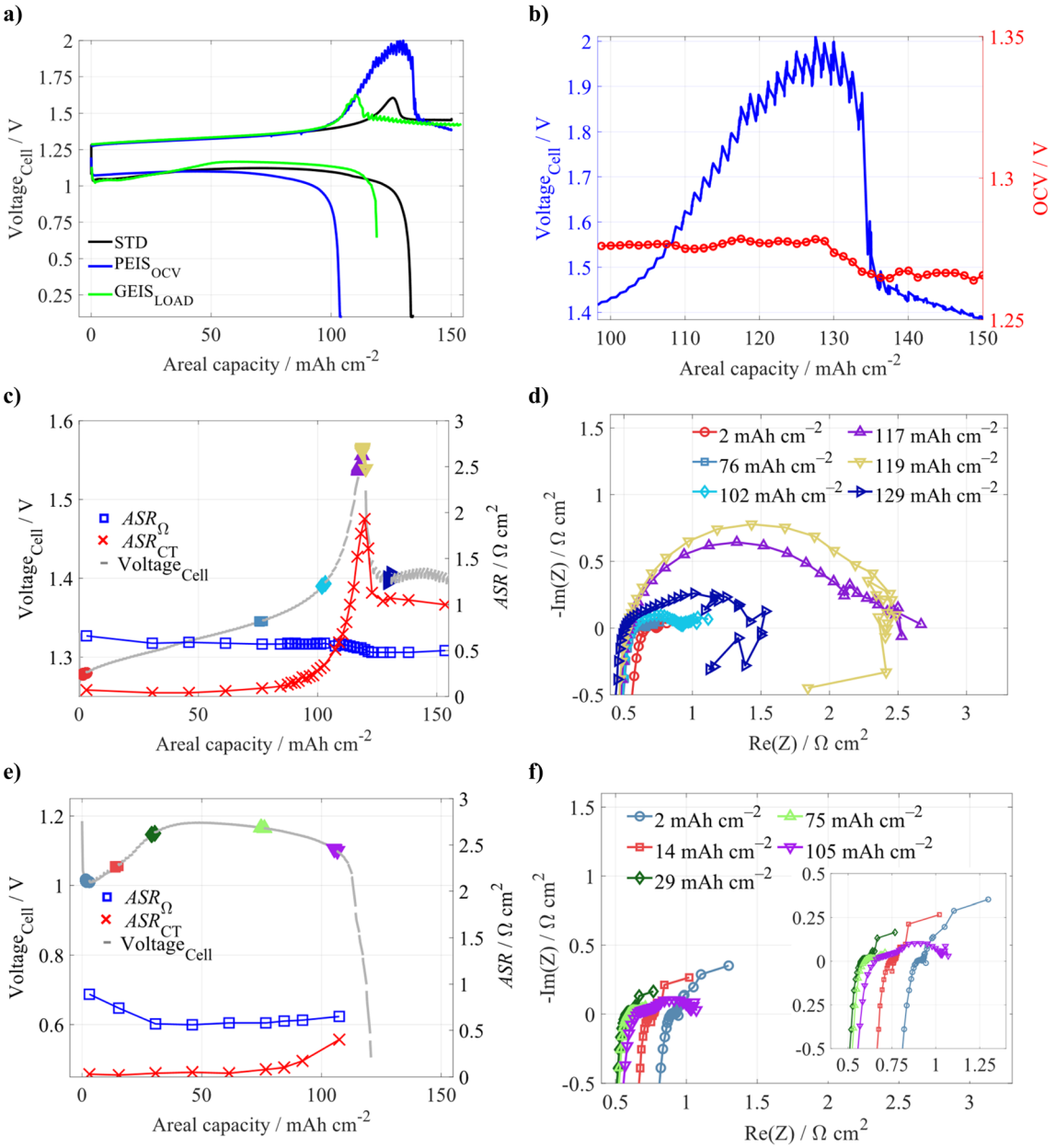

Fig. 5 (a) U-Q_{areal} dependence of a charge–discharge cycle for different characterization techniques: STD, PEIS$_{OCV}$, and GEIS$_{LOAD}$. (b) OCV$_{Cell}$-Q_{areal} dependence during PEIS$_{OCV}$ characterization. (c) U-Q_{areal} dependence during GEIS$_{LOAD}$ characterization with evaluated ASR$_{CT}$ and ASR$_{\Omega}$. The colours used in the voltage cell evolution are linked to (d), where EIS spectra are displayed with colours corresponding to Q_{areal}. (e and f) represent the same as (c and d), but for battery discharge. Experimental conditions: standard electrolyte composition, electrolyte volumes: 0.07 dm^3; current density: 100 mA cm^{-2}; operating temperature: 40 °C; electrolyte flow rate: 0.08 dm^3 min^{-1}.

measurements), while the discharged capacity is even further decreased, resulting in a low CE of only 70%. This is probably due to a longer pause between the charge and discharge parts of the cycle, and also pauses during which the PEIS$_{OCV}$ was measured (each PEIS$_{OCV}$ measurement required more than 10 minutes, *i.e.* the whole charge–discharge cycle took more than 13 hours, while the standard cycle took only 3 hours). Interestingly, for a given Q_{areal}, we observed significant variation of the EIS spectra with time (see Fig. S8). This is most probably linked with the surface passivation of zinc deposited at the negative electrode; however, a more detailed study is needed to confirm the hypothesis, which is beyond the scope of our study. Additionally, the quality of EIS spectra was significantly decreased at higher Q_{areal} (specifically in the low frequency region), due to insufficient stability of the system. Therefore, PEIS$_{OCV}$ characterization was found to be unsuitable for our purposes. Interestingly, we observed a visible drop of OCV$_{Cell}$ (see the red curve in Fig. 5b), although relatively small (approx. 14 mV), starting at the Q_{areal} corresponding to the voltaic bulge peak, suggesting changes in the composition of the electrolyte

 This journal is © The Royal Society of Chemistry 2025

Open Access Article. Published on 09 December 2025. Downloaded on 23/12/2025 23:59:47.
This article is licensed under a Creative Commons Attribution 3.0 Unported Licence.

and/or electrodes. The observed decrease in OCV_{Cell} can be attributed to membrane damage, which allows direct exposure of the deposited zinc to the posolyte containing tri-iodides, leading to enhanced self-discharge. However, as the majority of the zinc electrode remains intact and the bulk negolyte composition is largely preserved, the overall change in OCV_{Cell} remains rather small.

To mitigate the influence of battery behaviour instability during $PEIS_{OCV}$ measurements, the $GEIS_{LOAD}$ measurement was performed under constant current density load. The $GEIS_{LOAD}$ technique allows us to measure the EIS spectra simultaneously with CC charging/discharging of the battery, thereby suppressing the effect of zinc electrode changes during periods without current loading. Fig. 5a compares the cell voltage profiles for standard (STD) charging, $PEIS_{OCV}$, and $GEIS_{LOAD}$. The overvoltage development observed during $GEIS_{LOAD}$ closely resembles that of STD charging conditions. However, the voltaic bulge appeared even at lower Q_{areal}, which may be attributed to the alternating current applied during the $GEIS_{LOAD}$ measurement (*i.e.* current densities oscillated around 100 mA cm^{-2}). Nevertheless, the bulge's position varied slightly across the measurements even under standard conditions, typically occurring between 115 and 130 mAh cm^{-2}, thus both STD and $GEIS_{LOAD}$ experiments can be considered comparable.

More importantly, a significant increase in the ASR_{CT} is observed for the GEIS $_{LOAD}$ experiment (see Fig. 5c and d), starting at around 130 mAh cm^{-2}. The ASR_{CT} peak position aligns with the overvoltage maximum, and it subsequently decreases, stabilizing at approximately 1 Ω cm^2. In contrast, ASR_{Ω} gradually decreases in the same capacity region, with the most pronounced drop occurring near the voltage peak, after which it remains relatively constant. The decreased ASR_{Ω} aligns well with the hypothesis that the membrane is pierced by Zn dendrites.

Interestingly, the presence of a voltaic bulge also affects the battery overvoltage at the beginning of subsequent discharging. Fig. 5e shows a significant drop in battery voltage during the initial discharging phase, caused by ASR_{Ω} increase (blue curve, compared to the ASR_{Ω} at the end of charging), probably due to zinc electrode passivation (most probably related to the presence of tri-iodide ions). During the subsequent battery discharge, ASR_{Ω} decreases back to 0.6 Ω cm^2 after approx. 25 mAh cm^{-2} and, further on, the discharge voltage is similar to the experiment with the lower volume of negolyte (see Fig. 4a). ASR_{CT} increases when the battery is almost fully discharged, *i.e.* the zinc is almost fully dissolved.

To test the integrity of the membrane after the cycling, a tightness test was carried out (after the ZIHFB single-cell was emptied). One of the half-cells of the ZIHFB was pressurized by nitrogen, then hydraulically closed, and the rate of its pressure decay was monitored. In an initial cell with a fresh membrane, the pressure decayed at a slow rate of approximately 0.01 mbar s^{-1}, even under an overpressure of 600 mbar. In contrast, for the cell after the experiments, we observed significantly faster pressure drops of 0.32 mbar s^{-1}, indicating a decreased membrane tightness, most probably due to its perforation by Zn dendrites.

3.2.1 Influence of electrolyte composition: ZnI_2 omission in the posolyte. The composition of flow battery electrolytes plays a significant role in energy density, efficiency, and stability of storage. In the ZIHFB, Zn^{2+} ions are, in theory, only needed in the negolyte, while iodides are in the posolyte. However, in practice, the mixed electrolyte concept is typically used, containing both discharged active species in both electrolytes, which provides the battery with a favourable option of electrolyte remixing to restore the initial composition.

To further deepen our insight into the phenomena related to the voltaic bulge, we performed a similar set of experiments, but with ZnI_2 omitted from the posolyte. In the $PEIS_{OCV}$ experiment, we observed that the battery voltage during the charging increased earlier approximately at 100 mAh cm^{-2}, and a sudden voltage drop occurred later (purple curve in Fig. 6a) compared to the standard operation with Zn^{2+} in both electrolytes (black curve). Moreover, the behaviour of the OCV_{Cell} also differed: instead of stabilizing, the OCV_{Cell} continued to rise and only dropped when the overvoltage decreased (see Fig. 6b). As Zn^{2+} ions were absent in the posolyte for this experiment, they could not be supplied to the negative half-cell during the charging, unlike in the standard electrolyte set-up. At higher Q_{areal}, when the GF is plated with a compact zinc layer preventing the ion transport to a significant part of the electrode, the additional supply of Zn^{2+} from the posolyte is missing, which, in turn, results in a premature voltage increase in case of the $PEIS_{OCV}$ experiment.

However, in the case of $GEIS_{LOAD}$ cycling, the absence of Zn^{2+} in the posolyte appears to delay the voltaic bulge, shifting it to higher Q_{areal} values (~150 mAh cm^{-2}) (see Fig. 6a) when compared to both standard operation (black curve, with Zn^{2+} in the posolyte and without frequent EIS measurement) and $PEIS_{OCV}$. Although ASR_{Ω} remains approximately constant at the onset of the bulge, ASR_{CT} sharply increases in this region (see Fig. 6c). However, ASR_{CT} does not decrease significantly with the voltage drop – only a slight reduction is observed. This behaviour can be explained by partial membrane penetration by Zn dendrites (reflected in the decreased ASR_{Ω}) and partial zinc dissolution by tri-iodide ions. However, as Zn^{2+} is absent in the posolyte, the Zn deposition cannot proceed in the positive half-cell, as was possible for the standard electrolyte configuration, and thus, ASR_{CT} remains constant.

In general, the absence of Zn^{2+} in the posolyte allows pushing of the voltaic bulge to higher Q_{areal} and also reduction of the discharge overvoltage (see Fig. 6a). However, at the same time, a different initial composition of the posolyte and negolyte would inevitably lead to premature battery failure, primarily due to a significant cross-over of water, active species, and other ions through the membrane, which gradually changes the electrolyte composition (electrolyte volume imbalance is demonstrated in Fig. S9). The fluxes for symmetrical electrolyte composition are discussed in Section 3.1.2. In principle, the behaviour in this modified configuration will remain similar; however, as mentioned at the beginning of this section, with the initially equal electrolyte composition, the capacity fade due to membrane cross-over can be easily recovered by simple

Open Access Article. Published on 09 December 2025. Downloaded on 23/12/2025 23:59:47.
This article is licensed under a Creative Commons Attribution 3.0 Unported Licence.

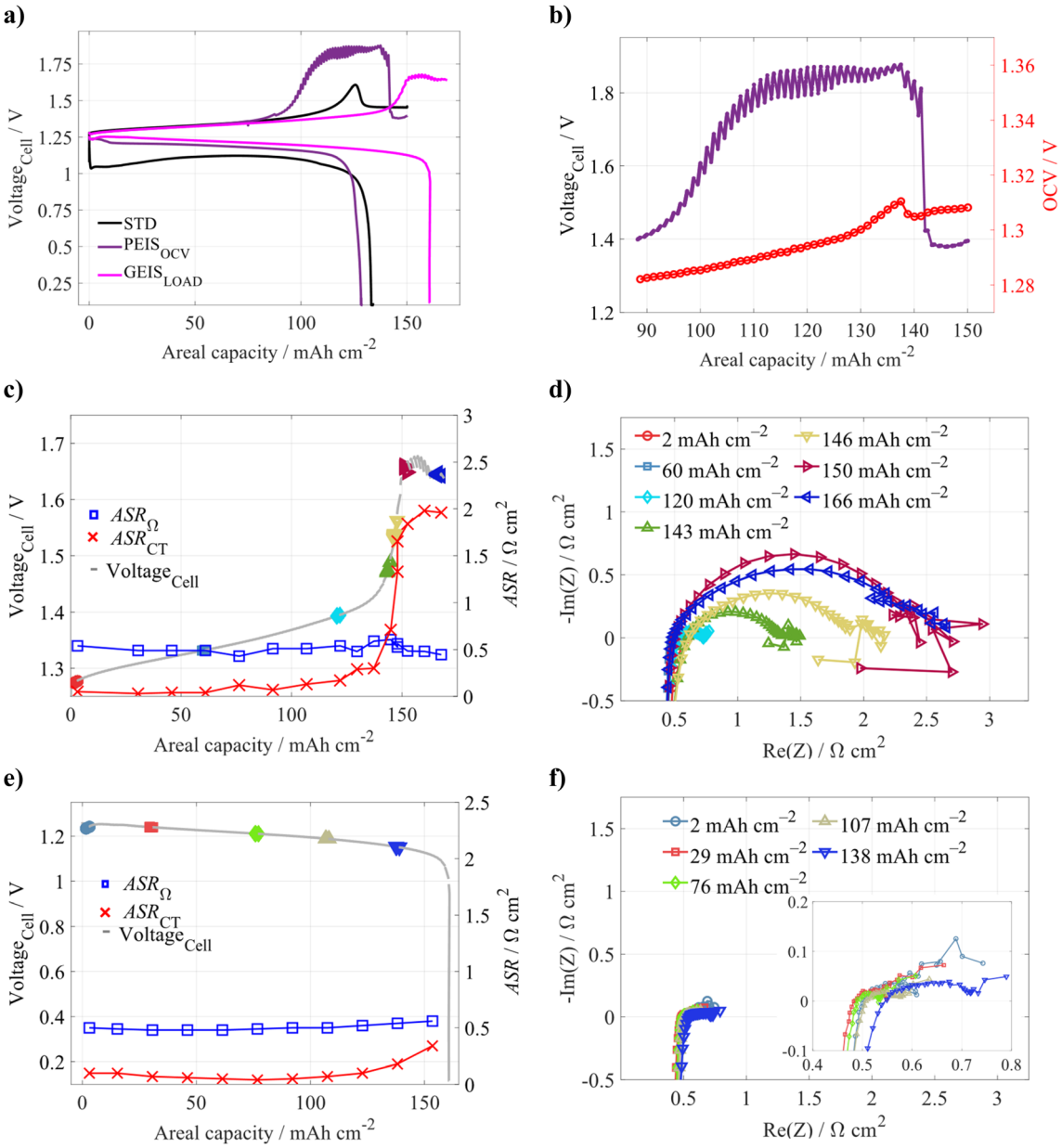

Fig. 6 (a) U-Q_{areal} dependence of a charge–discharge cycle for different characterization techniques: STD, PEIS$_{OCV}$ and GEIS$_{LOAD}$ for a ZIHFB with omitted zinc ions in the posolyte (besides STD). (b) OCV$_{Cell}$ dependence on Q_{areal} during PEIS$_{OCV}$ characterization. (c) U-Q_{areal} dependence during GEIS$_{LOAD}$ characterization with evaluated ASR$_{CT}$ and ASR$_{\Omega}$. The colours used in the voltage cell evolution are linked to (d), where EIS spectra are displayed with colours corresponding to Q_{areal}. (e and f) represent the same as (c and d), but for battery discharge. Experimental conditions: standard negolyte composition, ZnI_2 omitted from the posolyte (besides STD); both electrolyte volumes are 0.07 dm^3.

remixing of the electrolytes. For the posolyte without ZnI_2, this measurement is no longer possible.

3.3 Strategies for capacity regeneration

Subsequently, with the degraded battery, we tested several strategies that are typically used for an RFB to restore its initial capacity, namely: (i) electrolyte remix, (ii) exchange of both electrolytes for fresh ones, and (iii) exchange of the CEM (while keeping the same electrolytes). In this series of experiments, the volume of the electrolytes was decreased to 0.06 dm^3.

3.3.1 Electrolyte remixing and exchange. The first strategy tested for regenerating the battery performance was mixing the posolyte and negolyte and redistributing them. This procedure for regenerating the initial composition of the electrolytes is possible thanks to their initial equal composition. Electrolyte remix was done after complete ZIHFB discharge, and the whole procedure is described in detail in the subchapter in Section 2.2.3.

During the subsequent battery cycling, CE remained low, even for lower SoC charging limits (starting from 40% SoC, see Fig. 7a). Interestingly, in the first cycle after the electrolyte

 This journal is © The Royal Society of Chemistry 2025

Open Access Article. Published on 09 December 2025. Downloaded on 23/12/2025 23:59:47.
This article is licensed under a Creative Commons Attribution 3.0 Unported Licence.

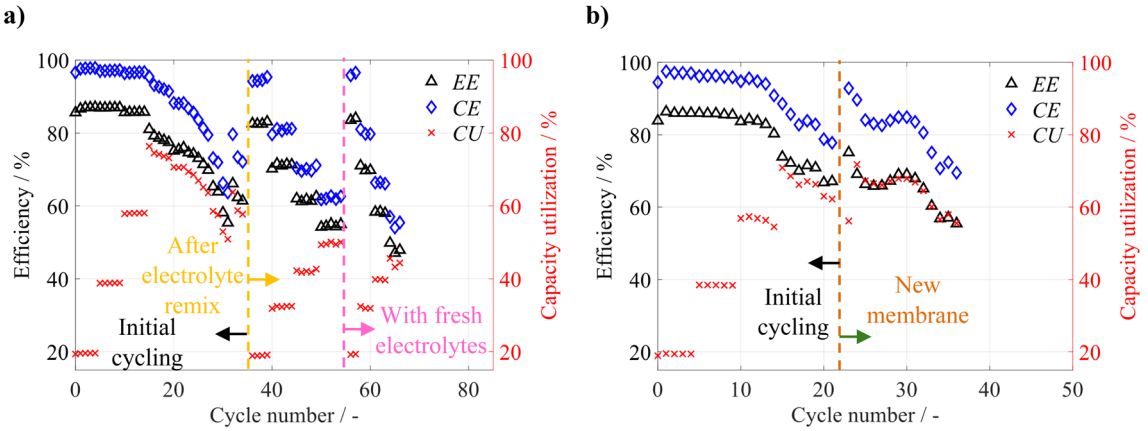

Fig. 7 Efficiencies and CU development (a) for the experiment with remix of the electrolyte and exchange of the electrolytes, and (b) for the experiment with CEM exchange. Experimental conditions: standard electrolyte composition; electrolyte volumes: 0.06 dm^3; current density: 100 mA cm^{-2}; operating temperature: 40 °C; electrolyte flow rate: 0.08 dm^3 min^{-1}.

remix, a low charging voltage was observed, *i.e.* a short plateau at 0.1 V at the beginning of charging (0–5 mAh cm^{-2}, see Fig. S10), which was caused by the reduction of tri-iodide ions at the negative half-cell. The tri-iodide presence in the remixed negolyte was a consequence of a faradaic imbalance between both electrolytes before the remix due to the coulombic inefficiency of the negative half-cell reaction (HER side reaction, self-discharge due to Zn corrosion) and accumulation of tri-iodide ions in the discharged posolyte. Even after a complete electrolyte exchange for fresh electrolytes, the original CE was not restored (depicted on the right side of Fig. 7a), which indicates that CEM damage is responsible for the irreversible performance fade.

3.3.2 Membrane exchange. To confirm the CEM damage, we repeated the experiment described above with fresh electrolytes and a new cell. The procedure initially involved increasing the SoC until the characteristic voltaic bulge appeared. Following this, the battery was fully discharged, and the electrolyte was remixed, as previously outlined. Then, the used CEM was replaced with a fresh one, while leaving the rest of the battery components unchanged (including GFs and both electrolytes). In Fig. 7b, we can see that the CEM replacement led to a substantial recovery of the CE to 90%, clearly proving that the membrane degradation is mostly responsible for cell performance degradation related to the voltaic bulge. However, during subsequent cycling, the CE dropped again; already in the second cycle, the voltaic bulge was observed (despite the charging voltage cut-off limit being set to 1.55 V), resulting again in CEM damage and a gradual decrease in discharge capacity. Lower CU after electrolyte exchange was caused by the presence of tri-iodide ions in the remixed negolyte, as discussed in the previous section.

3.4 Construction modifications

Based on our findings that the voltaic bulge is caused by deposition of a compact zinc layer near the electrode-membrane interface and the consequent perforation of the CEM by Zn dendrites, we tested several protection construction modifications of the battery cell and experimental set-up. These modifications aimed to mitigate the unwanted degradation mechanism and increase Q_{areal}, ensuring stable and efficient battery operation.

3.4.1 Non-conductive felt. Kellamis *et al.*[21] used NCF to increase the Q_{areal} in ZIHFB operation and prevent short circuits. We adopted a similar approach by combining electronically conductive GF and NCF (polymeric non-conductive felt, FINET PES 1 mm, MITOP) in each half-cell separately. This allowed us to investigate the effect of this construction modification on cell behaviour at increased Q_{areal}, aiming to at least partially suppress this phenomenon or to postpone it to higher Q_{areal}. The NCF was always in direct contact with the CEM, which was supposed to provide better protection of the membrane against Zn dendrites (for detailed schematics, see Fig. S2).

3.4.1.1 NCF in the negative half-cell. Initially, the combination of GF and NCF (close to the membrane) was used in the negative half-cell (for short NCF_{NEG}), so the initial deposition zone is more distant from the membrane (aiming to protect the membrane). Surprisingly, the use of NCF_{NEG} reduced CE by 3–4% for all the tested charging SoC limits (see Fig. 8a) when compared to standard battery construction (*i.e.* both half-cells using only conductive GF). This is probably a consequence of non-homogeneous growth of Zn in the NCF_{NEG} structure at relatively high applied current density (100 mA cm^{-2}), leading to its uneven distribution (a photo of NCF_{NEG} after the cycling is shown in Fig. S11) forming undesirable dendritic structures that are more susceptible to parasitic processes such as hydrogen evolution, Zn passivation and physical disintegration from the electrode bulk. Thus, in contrast to our expectations, the application of NCF_{NEG} did not suppress the voltaic bulge, nor did it shift it to higher Q_{areal} (see the blue curve in Fig. 8b).

A possible explanation for the presence of the voltaic bulge in the case of NCF_{NEG} is that a compact layer of zinc grows near the GF/NCF interface, which may have a similar insulating effect for ion transport between both half-cells of the battery, increasing

Open Access Article. Published on 09 December 2025. Downloaded on 23/12/2025 23:59:47.
This article is licensed under a Creative Commons Attribution 3.0 Unported Licence.

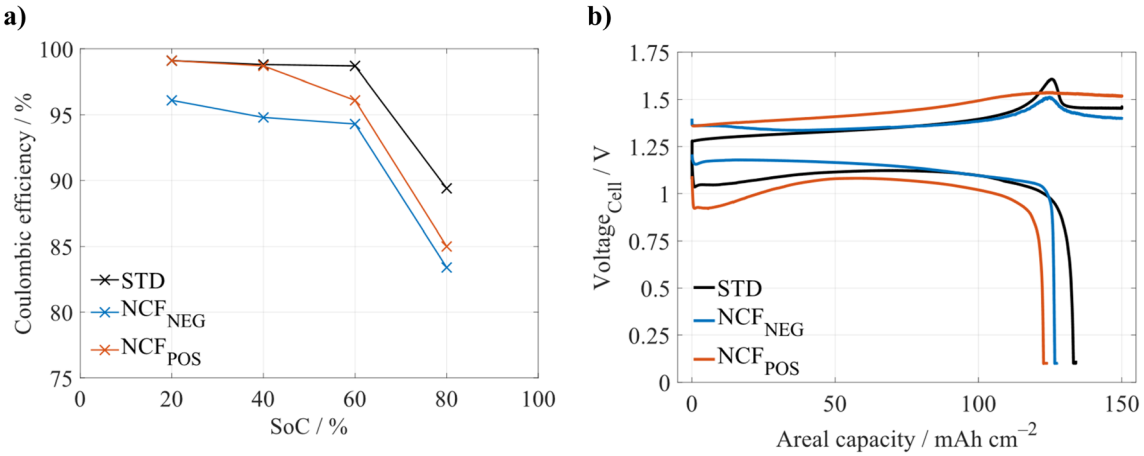

Fig. 8 (a) CE evolution for the standard construction and the experiment with the NCF_{NEG} and NCF_{POS} half-cell in the ZIHFB. (b) ZIHFB voltage dependence on Q_{areal} for different construction modifications (the construction modification is captioned in Fig. S2). Experimental conditions: standard electrolyte composition: 0.07 dm^3 of negolyte, 0.08 dm^3 of posolyte; current density: 100 mA cm^{-2}; operating temperature: 40 °C; electrolyte flow rate: 0.08 dm^3 min^{-1}.

local current densities and, in turn, resulting in more pronounced zinc dendrite formation and CEM perforation. In contrast to standard cell construction, interestingly, there is no increase in the overvoltage at the beginning of the discharging, which can be attributed to the fact that the compact zinc layer is located at the GF/NCF interface (*i.e.* not in direct contact with the CEM), and thus, a smaller portion of the CEM cross-sectional area is blocked. A higher discharge voltage is demonstrated with increased VE by 5% (see Table 2). The voltaic bulge occurs at approximately the same Q_{areal} (*i.e.* 125 mAh cm^{-2}) as for the standard electrode configuration, suggesting that the maximal capacity is limited by the inner geometry of the cell rather than the distribution of conductive and non-conductive phases in the negative half-cell.

3.4.1.2 NCF in a positive half-cell. In the next experiment, an NCF was used in a positive half-cell (again facing the membrane, for short NCF_{POS}). According to Kellamis *et al.*,[21] this approach should mitigate electric short circuits and thus lead to increased Q_{areal}. In our experiment, the voltaic bulge was present (see Fig. 8b), even though it was not that significant, and its position was similar to the STD and NCF_{NEG}, and irreversible reduction of the battery CE also occurred. The initial drop in discharge voltage was similar to a standard cell construction experiment, indicating that this effect is associated with the negative half-cell, as this voltage drop was absent in the NCF_{NEG} configuration. Due to the presence of an NCF_{POS} next to the CEM, providing a few mm thick electronically insulating zone, we can argue that the irreversibly reduced CE is not caused by a standard internal battery short circuit, *i.e.* the electron-conductive connection of the two electrodes. More probably, the zinc growing through the membrane is being continuously dissolved by the I_3^- present in the posolyte. This self-discharging process leads to a decreased CE, and its further gradual decrease due to the membrane perforation by Zn dendrites (after whose dissolution, holes remain in the membrane). Alternatively, some of the I_3^- may penetrate these pores and also dissolve the zinc deposited in the negative half-cell.

Table 2 shows a generally lower VE of the NCF_{POS} cell due to the significant increase in ASR_Ω (EIS measured at 50% SoC) caused by the presence of the electronically insulating NCF. Interestingly, in the NCF_{NEG} experiment, no significant increase in ASR_Ω was observed. This is because, upon charging, zinc is present within the negative electrode structure (both in GF and NCF), increasing the initially low conductivity of the NCF layer. Initial charging overvoltage for both NCF experiments is similar, and it decreases with increasing Q_{areal} for the arrangement with NCF_{NEG} (see the blue and orange curves in Fig. 8b), which confirms that the deposited zinc compensates the increased ASR_Ω.

Despite using similar construction modifications (NCF_{POS}) as in Kellamis *et al.*,[21] we did not reproduce their increase of Q_{areal}, potentially because we used conductive GF in the negative half-cell instead of NCF_{NEG}, as in their study. Other factors, such as the use of a different electrolyte composition (they used $ZnCl_2$ and NH_4Br), may cause the difference. Additionally, if we look at their results, we can see that during the initial 10 cycles, the available Q_{areal} decreased by more than 35% from the original 490 mAh cm^{-2}, due to the significant increase in the charging voltage and presence of zinc oxide in the negative half-

Table 2 ASR_Ω evaluated from EIS measured for 50% SoC and average CE and VE evaluated from the cycling with different SoC charging limits. The experimental conditions are the same as those given for Fig. 8

		SoC 60%		SoC 80%	
	ASR_Ω/Ω cm^2	CE/%	VE/%	CE/%	VE/%
Standard	0.68	98.7	78.4	89.4	76.4
NCF_{NEG}	0.60	94.3	83.4	83.4	81.1
NCF_{POS}	1.54	96.1	70.9	85.0	69.6

This journal is © The Royal Society of Chemistry 2025

Open Access Article. Published on 09 December 2025. Downloaded on 23/12/2025 23:59:47.
This article is licensed under a Creative Commons Attribution 3.0 Unported Licence.

cell. Thus, a similar trend was observed as in our system: a significant increase in charging voltage consequently affecting the discharge voltage. Nevertheless, the battery was not permanently damaged, likely due to the implementation of a safety charging voltage limit.

3.4.2 Hydraulic connection of electrolyte tanks. Finally, we identified stable operating conditions for the ZIHFB single-cell by combining a safety charging cut-off voltage and a reduced charging Q_{areal} limit (for detailed conditions see the subchapter in Section 2.2.3) with a hydraulic connection between the electrolyte tanks. HS was used to maintain equal electrolyte volumes and to at least partially equalize their composition *via* a thin capillary at the bottom of the tanks. This strategy is typically used in a VRFB to maintain constant electrolyte volumes, mitigating the capacity fade due to active species cross-over.[37]

In a ZIHFB with a CEM, the net ion and water flux during charging are directed from the posolyte to the negolyte, reversing during discharge, as discussed in Section 3.1.2. When an HS is present, the reverse flow through the HS partially compensates for these volume changes and, to some extent, mitigates composition imbalances during battery operation. However, this benefit comes at the expense of reduced CE due to increased self-discharge (zinc dissolution by tri-iodide ions transferred *via* HS from the posolyte); however, this can prevent excess zinc accumulation and associated risks.

First, the standard apparatus without HS of electrolyte tanks was used to study the effect of HS on the operation of the ZIHFB. Despite the safety limits applied, the operation of the battery without HS was unstable. As shown in Fig. 9a, the battery exhibits a gradual decrease in all efficiencies during CC cycling periods, which can probably be attributed to zinc accumulation (its incomplete dissolution during discharge periods), which caused the battery to operate at gradually increased SoC (of the negolyte), leading to increased charging voltage. During the two formatting cycles (CC charge and combined CC–CV discharge), a steep recovery of CE was observed, indicating that the accumulated zinc was effectively dissolved by potentiostatic discharge at 0.1 V. However, the improvement was only temporary as the voltaic bulge appeared after approximately 48 cycles (80 hours), and the battery was irreversibly degraded. The voltaic bulge appeared due to the changing electrolyte composition caused by notable electrolyte cross-over (from the posolyte to the negolyte, as shown in Fig. S12).

The deployment of HS led to significant stabilization of the battery operation (see stable efficiency development in Fig. 9b), due to continuous balancing of the electrolyte's volumes (and partially also of their composition). Most likely, some of the accumulated zinc was also partially dissolved during discharge by the I_3^-, which was gradually transported to the negolyte *via* HS. In other words, continuous mitigation of zinc accumulation in the negative half-cell prevents overcharging of the battery (*i.e.*, exceeding critical Q_{areal}) and protects against subsequent membrane damage. With these optimized conditions, the ZIHFB was operated at 100 mA cm^{-2}, achieving high performance, demonstrated by VE and EE being consistently above 80%, while no significant performance deterioration was observed.

We found that from the mitigation strategies tested, a mid-term stable and efficient battery operation (at least in our configuration) can only be achieved by decreasing the charging Q_{areal} limit (to 50% SoC, Q_{areal} 80 mAh cm^{-2}), applying a voltage charging limit (1.55 V) and, most importantly, implementing HS construction modification for mutual connection of the electrolyte tanks. The achieved Q_{areal} of 80 mAh cm^{-2} at a high current density of 100 mA cm^{-2} is higher than in most of the literature, where the reported Q_{areal} values are between 40 and 60 mAh cm^{-2} (ref. 29, 34, 38 and 39) for current densities no higher than 80 mA cm^{-2}. Only one study by Kellamis *et al.*[21] reported higher Q_{areal} (stable above 350 mAh cm^{-2}), thanks to the use of NCF_{POS}, as discussed in a previous chapter. However, our configuration excels in terms of high efficiencies (EE is higher by 24% in our configuration) and improved safety (bromine-free), and can be used for power applications with lower capacity.

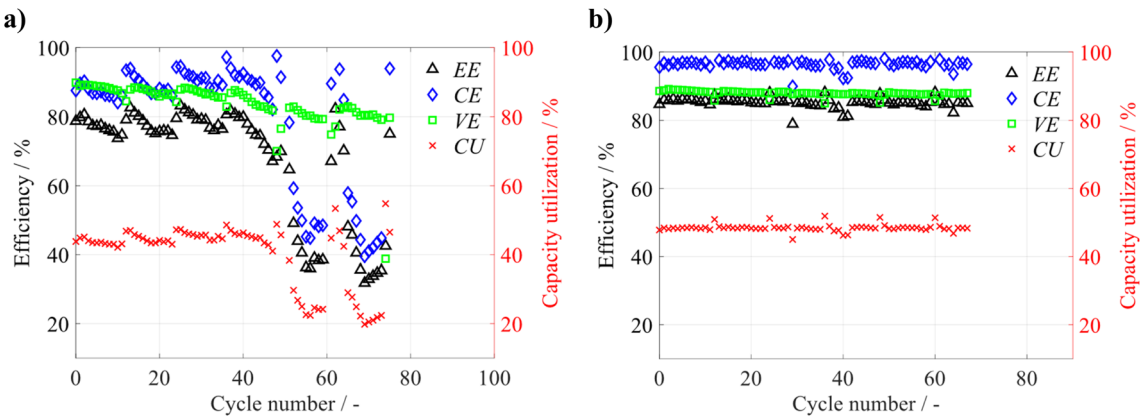

Fig. 9 Comparison of efficiency development in the ZIHFB under optimized operation conditions: (a) without HS and (b) with HS. Experimental conditions: standard electrolyte composition; electrolytes volumes: 0.06 dm^3; charging voltage limit: 1.55 V; Q_{areal} capacity charge limit: 80 mAh cm^{-2}; current density: 100 mA cm^{-2}; operating temperature: 40 °C; electrolyte flow rate: 0.08 dm^3 min^{-1}.

Open Access Article. Published on 09 December 2025. Downloaded on 23/12/2025 23:59:47.
This article is licensed under a Creative Commons Attribution 3.0 Unported Licence.

Besides the promising performance parameters achieved, as mentioned above, the main contribution of our study is the proposed and experimentally validated mechanistic explanation of the voltaic bulge phenomenon and its consequences for battery operation. These findings highlight the importance of further R&D of this system, which should aim to improve the homogeneity of the Zn distribution within the 3D negative electrode, *e.g.* by variation of its surface chemistry, conductivity and texture in order to further increase the Q_{areal} of the ZIHFB cell and to decrease the cost per capacity related to battery stacks.

4. Conclusions

In this study, we investigated a degradation phenomenon in ZIHFBs, referred to as the voltaic bulge, which occurs when charging to high Q_{areal}. This effect manifests itself as a sharp voltage increase followed by a sudden drop, resulting in an irreversibly decreased CE of the charge–discharge cycle. Although the bulge gradually disappears upon further cycling, it is accompanied by irreversible damage to the ion-exchange membrane, requiring replacement to restore the initial battery performance. Our results suggest that, for the standard cell construction, the bulge originates from the formation of a compact zinc layer near the electrode-membrane interface, restricting ion transport from the positive to negative electrode and increasing local current densities at the negative half-cell, which promotes dendritic growth and membrane perforation. For our system, the phenomenon typically appears at a critical Q_{areal} of 115–130 mAh cm^{-2} and is promoted by the presence of Zn^{2+} in the posolyte (*i.e.* for equal initial compositions of both electrolytes). Removing Zn^{2+} from the posolyte delays its onset to higher capacities, but it does not represent a viable long-term solution due to mutual electrolyte cross-contamination and early battery failure. From the tested construction modifications, the application of non-conductive felt to individual half-cells did not increase the limiting Q_{areal}, while hydraulic connection of the electrolyte tanks significantly improved the performance stability within restricted SoC limits. Safe operating conditions were identified as a charging voltage limited to 1.55 V and a maximum charging Q_{areal} of 80 mAh cm^{-2}. The system with the optimized construction (HS) and operating conditions enabled stable cycling with CE $\geq$ 95% and EE > 83% at 100 mA cm^{-2} and a low-capacity fade of 0.02% per cycle. Understanding the mechanism provides a basis for strategies to mitigate membrane degradation and improve the durability of ZIHFBs and related zinc-based chemistry.

Author contributions

Přemysl Richtr: writing – original draft, investigation, formal analysis, validation, methodology, conceptualization, data curation, writing – review & editing. David Gráf: investigation, visualization, writing – review & editing. Martin Drnec: investigation. Jiří Charvát: conceptualization, writing – review & editing. Martin Bureš: software, writing – review & editing, software. Ondřej Navrátil: conceptualization. Jaromír Pocedič: supervision, conceptualization. Juraj Kosek: project administration, funding acquisition. Petr Mazúr: project administration, supervision, funding acquisition, writing – review & editing, resources, conceptualization.

Conflicts of interest

There are no conflicts to declare.

Data availability

Data for this article are available at Zenodo at https://doi.org/10.5281/zenodo.17175636. This DOI represents all versions and will always resolve to the latest one.

Supplementary information (SI) is available. See DOI: https://doi.org/10.1039/d5ta07792c.

Acknowledgements

This work was supported by the project "The Energy Conversion and Storage", funded as project no. CZ.02.01.01/00/22_008/0004617 by Programme Johannes Amos Comenius, called Excellent Research. This work was supported by TAČR, program TREND, project no. FW06010097. This work was supported from the grant of Specific university research – grant A1_FCHI_2024_04 and A2_FCHI_2025_014.

References

1 L. Wang, *et al.*, Science mapping the knowledge domain of electrochemical energy storage technology: A bibliometric review, *J. Energy Storage*, 2024, **77**, 109819.
2 T. M. Gür, Review of electrical energy storage technologies, materials and systems: challenges and prospects for large-scale grid storage, *Energy Environ. Sci.*, 2018, **11**(10), 2696–2767.
3 E. Sánchez-Díez, *et al.*, Redox flow batteries: Status and perspective towards sustainable stationary energy storage, *J. Power Sources*, 2021, **481**, 228804.
4 P. Arévalo-Cid, *et al.*, Redox flow batteries: a new frontier on energy storage, *Sustainable Energy Fuels*, 2021, **5**(21), 5366–5419.
5 K. Lourenssen, *et al.*, Vanadium redox flow batteries: A comprehensive review, *J. Energy Storage*, 2019, **25**, 100844.
6 P. Mazur, *et al.*, Effect of graphite felt properties on the long-term durability of negative electrode in vanadium redox flow battery, *J. Power Sources*, 2019, **414**, 354–365.
7 M. Skyllas-Kazacos and J. F. McCann, Chapter 10 – Vanadium redox flow batteries (VRBs) for medium- and large-scale energy storage, in *Advances in Batteries for Medium and Large-Scale Energy Storage*, ed. C. Menictas, M. Skyllas-Kazacos and T. M. Lim, Woodhead Publishing, 2015, pp. 329–386.
8 Á. Cunha, *et al.*, Vanadium redox flow batteries: a technology review, *Int. J. Energy Res.*, 2015, **39**(7), 889–918.

 This journal is © The Royal Society of Chemistry 2025

Open Access Article. Published on 09 December 2025. Downloaded on 23/12/2025 23:59:47.
This article is licensed under a Creative Commons Attribution 3.0 Unported Licence.

9 P. Leung, *et al.*, Progress in redox flow batteries, remaining challenges and their applications in energy storage, *RSC Adv.*, 2012, **2**(27), 10125–10156.
10 J. Noack, *et al.*, Techno-Economic Modeling and Analysis of Redox Flow Battery Systems, *Energies*, 2016, **9**(8), 627.
11 J. Noack, *et al.*, Studies on Fe/Fe Redox Flow Batteries with Recombination Cell, *J. Electrochem. Soc.*, 2020, **167**(16), 160527.
12 A. Mahmood, Z. Zheng and Y. Chen, Zinc–Bromine Batteries: Challenges, Prospective Solutions, and Future, *Advanced Science*, 2024, **11**(3), 2305561.
13 D. Fan, *et al.*, Progress and challenges of zinc-iodine flow batteries: From energy storage mechanism to key components, *J. Energy Storage*, 2024, **92**, 112215.
14 W. J. Jang, *et al.*, Effect of an Iodine Film on Charge-Transfer Resistance during the Electro-Oxidation of Iodide in Redox Flow Batteries, *ACS Appl. Mater. Interfaces*, 2021, **13**(5), 6385–6393.
15 J. Dundálek, *et al.*, Zinc electrodeposition from flowing alkaline zincate solutions: Role of hydrogen evolution reaction, *J. Power Sources*, 2017, **372**, 221–226.
16 X. G. Zhang, Secondary Batteries – Zinc Systems | Zinc Electrodes: Overview, in *Encyclopedia of Electrochemical Power Sources*, ed. J. Garche, Elsevier, 2009, Amsterdam, pp. 454–468.
17 W. Lu, *et al.*, Anode for Zinc-Based Batteries: Challenges, Strategies, and Prospects, *ACS Energy Lett.*, 2021, **6**(8), 2765–2785.
18 F. ShakeriHosseinabad, *et al.*, Influence of Flow Field Design on Zinc Deposition and Performance in a Zinc-Iodide Flow Battery, *ACS Appl. Mater. Interfaces*, 2021, **13**(35), 41563–41572.
19 B. Pichler, *et al.*, The impact of operating conditions on component and electrode development for zinc-air flow batteries, *J. Appl. Electrochem.*, 2018, **48**(9), 1043–1056.
20 D. P. Trudgeon, *et al.*, Screening of effective electrolyte additives for zinc-based redox flow battery systems, *J. Power Sources*, 2019, **412**, 44–54.
21 C. J. Kellamis and J. S. Wainright, A zinc–iodine hybrid flow battery with enhanced energy storage capacity, *J. Power Sources*, 2024, **589**, 233753.
22 Z. Xu, *et al.*, Review of zinc dendrite formation in zinc bromine redox flow battery, *Renewable Sustainable Energy Rev.*, 2020, **127**, 109838.
23 M. Bockelmann, U. Kunz and T. Turek, Electrically rechargeable zinc-oxygen flow battery with high power density, *Electrochem. Commun.*, 2016, **69**, 24–27.
24 P. Richtr, *et al.*, Nickel-cobalt spinel-based oxygen evolution electrode for zinc-air flow battery, *J. Energy Storage*, 2025, **115**, 115835.
25 Y. Zhao, *et al.*, Accelerating the dissolution kinetics of iodine with a cosolvent for a high-current zinc–iodine flow battery, *J. Mater. Chem. A*, 2022, **10**(26), 14090–14097.
26 J. Vrána, *et al.*, Commercial perfluorosulfonic acid membranes for vanadium redox flow battery: Effect of ion-exchange capacity and membrane internal structure, *J. Membr. Sci.*, 2018, **552**, 202–212.
27 L. Gubler, Membranes and separators for redox flow batteries, *Curr. Opin. Electrochem.*, 2019, **18**, 31–36.
28 J. Charvát, *et al.*, The role of ion exchange membrane in vanadium oxygen fuel cell, *J. Membr. Sci.*, 2021, **629**, 119271.
29 C. Xie, *et al.*, A Long Cycle Life, Self-Healing Zinc–Iodine Flow Battery with High Power Density, *Angew. Chem., Int. Ed.*, 2018, **57**(35), 11171–11176.
30 C. Xie, *et al.*, Highly stable zinc–iodine single flow batteries with super high energy density for stationary energy storage, *Energy Environ. Sci.*, 2019, **12**(6), 1834–1839.
31 G.-M. Weng, *et al.*, Unlocking the capacity of iodide for high-energy-density zinc/polyiodide and lithium/polyiodide redox flow batteries, *Energy Environ. Sci.*, 2017, **10**(3), 735–741.
32 P. Mazúr, *et al.*, Performance evaluation of thermally treated graphite felt electrodes for vanadium redox flow battery and their four-point single cell characterization, *J. Power Sources*, 2018, **380**, 105–114.
33 Y. Savsatli, *et al.*, In Situ and Operando Observation of Zinc Moss Growth and Dissolution in Alkaline Electrolyte for Zinc–Air Batteries, *ACS Energy Lett.*, 2024, **9**(7), 3516–3525.
34 M. Mousavi, *et al.*, Decoupled low-cost ammonium-based electrolyte design for highly stable zinc–iodine redox flow batteries, *Energy Storage Mater.*, 2020, **32**, 465–476.
35 J. Charvát, *et al.*, Performance enhancement of vanadium redox flow battery by optimized electrode compression and operational conditions, *J. Energy Storage*, 2020, **30**, 101468.
36 M. Bureš, *et al.*, Mathematical modeling of electric and hydraulic resistances of reconstructed carbon felt electrodes using micro-computed tomography, *Chem. Eng. J.*, 2023, **458**, 141424.
37 M. Bureš, *et al.*, Evaluation of mitigation of capacity decay in vanadium redox flow batteries for cation- and anion-exchange membrane by validated mathematical modelling, *J. Power Sources*, 2024, **591**, 233769.
38 Q. P. Jian, *et al.*, A trifunctional electrolyte for high-performance zinc-iodine flow batteries, *J. Power Sources*, 2021, **484**, 229238.
39 Y. Li, *et al.*, Homogenizing Zn Deposition in Hierarchical Nanoporous Cu for a High-Current, High Areal-Capacity Zn Flow Battery, *Small*, 2023, **19**(40), 2303005.